



## Supplemental Material

*Bulletin of the American Meteorological Society*  
Satellite-Based Ranking of the World's Hottest  
and Coldest Cities Reveals Inequitable  
Distribution of Temperature Extremes  
<https://doi.org/10.1175/BAMS-D-22-0233.2>

© Copyright 2023 American Meteorological Society (AMS)

For permission to reuse any portion of this work, please contact [permissions@ametsoc.org](mailto:permissions@ametsoc.org). Any use of material in this work that is determined to be "fair use" under Section 107 of the U.S. Copyright Act (17 USC §107) or that satisfies the conditions specified in Section 108 of the U.S. Copyright Act (17 USC §108) does not require AMS's permission. Republication, systematic reproduction, posting in electronic form, such as on a website or in a searchable database, or other uses of this material, except as exempted by the above statement, requires written permission or a license from AMS. All AMS journals and monograph publications are registered with the Copyright Clearance Center (<https://www.copyright.com>). Additional details are provided in the AMS Copyright Policy statement, available on the AMS website (<https://www.ametsoc.org/PUBSCopyrightPolicy>).

# **Satellite-based Ranking of the World's Hottest and Coldest Cities Reveals Inequitable Distribution of Temperature Extremes**

Jiufeng Li<sup>1</sup>, Wenfeng Zhan<sup>1,2\*</sup>, TC Chakraborty<sup>3</sup>, Zihan Liu<sup>1</sup>, Huilin Du<sup>1</sup>, Weilin Liao<sup>4</sup>, Ming Luo<sup>4</sup>, Long Li<sup>1</sup>, Shiqi Miao<sup>1</sup>, Huyan Fu<sup>5</sup>, Shasha Wang<sup>1</sup>, Fan Huang<sup>1</sup>, Manchun Li<sup>6</sup>

<sup>1</sup> Jiangsu Provincial Key Laboratory of Geographic Information Science and Technology, International Institute for Earth System Science, Nanjing University, Nanjing, Jiangsu 210023, China

<sup>2</sup> Jiangsu Center for Collaborative Innovation in Geographical Information Resource Development and Application, Nanjing, Jiangsu 210023, China

<sup>3</sup> Atmospheric Sciences and Global Change Division, Pacific Northwest National Laboratory, Richland, Washington, WA 99354, USA

<sup>4</sup> Guangdong Key Laboratory for Urbanization and Geo-simulation, School of Geography and Planning, Sun Yat-sen University, Guangzhou, Guangdong 510006, China

<sup>5</sup> Department of Geographic Information Science, School of Earth Sciences, Yunnan University, Kunming, Yunnan 650091, China

<sup>6</sup> School of Geography and Ocean Science, Nanjing University, Nanjing, Jiangsu 210023, China

*Corresponding author:* W. Zhan, zhanwenfeng@nju.edu.cn

## **This PDF file includes:**

Notes S1 to S8  
Figs. S1 to S21  
Tables S1 to S6  
References

### **Supplementary Note 1: *Uneven distribution of weather stations across global urban areas***

Combining the global weather stations provided by Berkeley Earth (<http://berkeleyearth.org/>) and the GHSL urban boundary data (refer to Methods), we find that urban and non-urban stations account for 9% and 91% of global available stations, respectively. The proportions of urban stations in the high-income (HIC), upper-and-middle income (UMIC), lower-and-middle-income (IMIC), and low-income (LIC) cities are 15%, 38%, 42%, and 5%, respectively (Fig. S2B). HIC cities account for 15% of all major cities, yet they possess 45% urban stations. By comparison, LMIC cities account for 42% of these cities, but they have only 15% urban stations (Fig. S2, B and C). The station density in HIC cities ( $1/123 \text{ km}^2$ , i.e., one urban station per  $123 \text{ km}^2$ ) is about twice of that in low-income cities ( $1/219 \text{ km}^2$ ; including UMIC, IMIC, and LIC cities). With such a contrast in station distribution and density over cities with different economic levels, it is therefore very difficult to identify the world's hottest and coldest cities.

## **Supplementary Note 2: Possible uncertainties related to the MODIS LST product**

The MODIS LST data product is currently considered the most appropriate satellite dataset to investigate urban thermal environment across global cities in a globally consistent fashion ( Clinton and Gong 2013; Chakraborty and Lee 2019; Si et al. 2022). The MODIS sensors provide daily acquisitions with a spatial resolution of ~1 km since 2001 (since 2003 for the Aqua satellite data used here), with the retrieval errors being mostly below 1.0 K over homogeneous surfaces (Wan et al. 2015). We acknowledge that the retrieval errors of the daily MODIS LST products can become relatively higher over urban areas due to urban thermal anisotropy (Jiang et al. 2021) and urban high heterogeneity (Clemens et al. 2021). However, these errors should be largely minimized through the data processing. We first temporally aggregated daily LST data into monthly composites (table S2) and then spatially aggregated these monthly composites into city mean values. This kind of spatiotemporal aggregation can considerably reduce the effects of urban thermal anisotropy and especially the random retrieval errors of the daily MODIS LST products. Note since some the systematic retrieval errors span the entire retrieval period, these would not be an issue in this study, since the LST is used as an input variable to model near surface-air temperature (NSAT).

**Supplementary Note 3: Overall and monthly validations for the monthly mean maximum and minimum NSATs across cities with different income levels**

We evaluated the root mean squared error (RMSE) and mean absolute error (MAE) of the ideal RF model for the cities with different income levels. The results suggest that the accuracy of the RF model is broadly consistent with that of previous studies (dos Santos 2020; Ho et al. 2014; Hooker et al. 2018; Verdin et al. 2020; Yoo et al. 2018). The RMSE/MAE of the monthly mean maximum NSAT for the low-income (LIC), lower-and-middle-income (LMIC), upper-and-middle-income (UMIC), and high-income (HIC) cities are  $1.22^{\circ}\text{C}/0.80^{\circ}\text{C}$ ,  $1.05^{\circ}\text{C}/0.76^{\circ}\text{C}$ ,  $1.19^{\circ}\text{C}/0.86^{\circ}\text{C}$ , and  $0.97^{\circ}\text{C}/0.71^{\circ}\text{C}$ , respectively (Fig. S15). The corresponding RMSE/MAE of the monthly mean minimum NSAT for LIC, LMIC, UMIC, and HIC are  $1.05^{\circ}\text{C}/0.71^{\circ}\text{C}$ ,  $0.94^{\circ}\text{C}/0.67^{\circ}\text{C}$ ,  $1.05^{\circ}\text{C}/0.75^{\circ}\text{C}$ , and  $0.98^{\circ}\text{C}/0.73^{\circ}\text{C}$ , respectively (Fig. S16).

**Supplementary Note 4: Validation and relative importance scores for the monthly mean maximum and minimum NSATs across Europe, North America, and China**

Here we tested the performance of the trained model across Europe, North America, and China. The results reveal that there is a slight difference in the accuracy among these three regions (Fig. S17). The RMSE/MAE of monthly mean maximum NSAT are  $1.05\text{ }^{\circ}\text{C}/0.74\text{ }^{\circ}\text{C}$ ,  $1.04\text{ }^{\circ}\text{C}/0.76\text{ }^{\circ}\text{C}$ , and  $0.96\text{ }^{\circ}\text{C}/0.72\text{ }^{\circ}\text{C}$ , respectively for Europe, North America, and China. Similarly, those for monthly mean minimum NSAT are  $1.05\text{ }^{\circ}\text{C}/0.73\text{ }^{\circ}\text{C}$ ,  $1.06\text{ }^{\circ}\text{C}/0.78\text{ }^{\circ}\text{C}$ , and  $0.86\text{ }^{\circ}\text{C}/0.63\text{ }^{\circ}\text{C}$ , respectively.

Fig. S18 reveals that the relative importance of these variables rarely changes across 12 months over Europe, North America, and China. We therefore calculated the annual mean values of these relative importance (Fig. S19). For Europe, North America, and China, the 2-m AT dominates the urban maximum NSAT while nighttime LST dominates the urban minimum NSAT (Fig. S19). This suggests that background climate variables and urban LST have a greater impact on urban maximum and minimum NSATs, respectively. Moreover, for both the urban maximum and minimum NSATs, the relative importance value of the 2-m AT in China is larger than that of Europe and North America, while for daytime/nighttime LST, the relative importance value in China is smaller than those of Europe and North America (Fig. S19). These regional differences imply a larger contribution from background climate in China while a larger urbanization-induced contribution in Europe and North America. One possible reason for this is the lower latitude of China and the higher urbanization level in Europe and North America. In addition, a considerable contribution of EVI homogeneity is found in these three regions (Fig. S19), indicating that the landscape patterns and vegetation diversity play a critical role in affecting urban maximum and minimum NSATs.

The contrasting relative importance of background climate and urban variables, as well as their slightly different performance across Europe, North America, and China, suggest that the designed random forest models may be constrained by potential physical components. Therefore, future efforts are still required to further incorporating more physical rules and advancing the capability of RF models to simulate climate extremes (O’Gorman and Dwyer 2018; Reichstein et

al. 2019). This could potentially improve further the accuracy and robustness of such models in estimating urban NSAT and other climate-related variables.

**Supplementary Note 5: Validation of the intra-urban variability of maximum and minimum NSATs across nine cities with relatively dense weather stations**

We validated the intra-city variability of  $NSAT_{\max}$  (for July) and  $NSAT_{\min}$  (for January) in nine cities with relatively dense weather stations for the years 2003, 2010, and 2019. The results reveal that the RF models possess relatively high accuracies and are capable of capturing intra-city temperature variability. Specifically, the mean RMSE and MAE of the monthly mean maximum NSAT for these nine cities are  $1.17^{\circ}\text{C}$  and  $0.82^{\circ}\text{C}$  respectively (Fig. S20), while those for the monthly mean minimum NSAT are  $1.99^{\circ}\text{C}$  and  $1.13^{\circ}\text{C}$  respectively (Fig. S20).

**Supplementary Note 6: *Relative importance of input variables for random forest models in estimating monthly mean maximum and minimum NSATs***

We find that the relative importance scores for the input variables remain largely stable across all months. The 2-m air temperature (2-m AT) has the highest mean relative importance (i.e., 15.33%) in estimating monthly mean maximum NSAT, followed by the secondary one of 11.75% for daytime LST (Fig. S21). Besides, both downward surface solar radiation (DSSR) and downward surface thermal radiation (DSTR) contribute to a considerable percentage of the relative importance compared to the remaining factors. This indicates that the intra-city maximum NSAT is dominated by background climate variables, with a secondary role for the input variables related to intra-city surface thermal property such as daytime LST. In contrast, the mean relative importance of nighttime LST is larger than that of 2-m AT, DSTR, and DSSR in estimating monthly mean minimum NSAT (Fig. S21). This implies that the monthly mean minimum NSAT is largely affected by intra-city surface thermal property rather than background climate variables. This makes sense because urban AT and LST tend to show stronger coupling during nighttime (Chakraborty et al. 2022).

**Supplementary Note 7: Reasons for using an empirical model based on the relative humidity-temperature index**

Empirical models derived from the relative humidity-temperature index have received wide popularity in the estimation of thermal discomfort and they have also been acknowledged in various official reports (Schoen 2005; NOAA, 2023; Weinberger et al. 2018). However, such empirical models may hold potential uncertainties because they do not incorporate the radiation components (such as mean radiation temperature, termed MRT). The MRT is subject to reflection and absorption of heat induced by the 3D structure, materials, and colors of urban buildings (Huang et al. 2014; Lindberg et al. 2008), yet it is a very challenging task to accurately derive urban MRT across global cities. Therefore, empirical models derived from the temperature-humidity index are still one of the more feasible means to estimate thermal discomfort, especially for large-scale studies.

**Supplementary Note 8: Possible uncertainties related to retrieval of relative humidity used for calculating thermal discomfort index**

This study calculated the thermal discomfort index (TDI) for global urban settlements by incorporating humidity information obtained from reanalysis data. We acknowledge that the incorporated reanalysis data-derived humidity may not be sufficiently accurate because of the absence of a true urban signal in reanalysis data (Balsamo et al. 2009; Bassett et al. 2021; Venter et al. 2021). In other words, the reanalysis data-derived humidity over urban areas may either be overestimated or underestimated due to urban dryness island effect (UDI) and urban moisture effect (UMI) respectively. Nevertheless, the UDI or UMI intensity is relatively small in terms of its impacts on local thermal discomfort (Du et al. 2022). The urban-rural difference in relative humidity is mostly lower than 10% or even lower (Meili et al. 2022). One recent study over rapidly urbanizing China demonstrates that the monthly mean UDI intensity is only 3.5% (Luo et al. 2021). More importantly, it is hard to derive accurate estimates of UDI intensity across global 13,135 settlements especially over cities in the Global South, although observations on relative humidity over some of the cities in the Global North do exist. Given these limitations, reanalysis data provide humidity information in a globally consistent way that can be used for a fair comparison across global cities. We therefore use reanalysis data-derived humidity information to calculate the TDI.

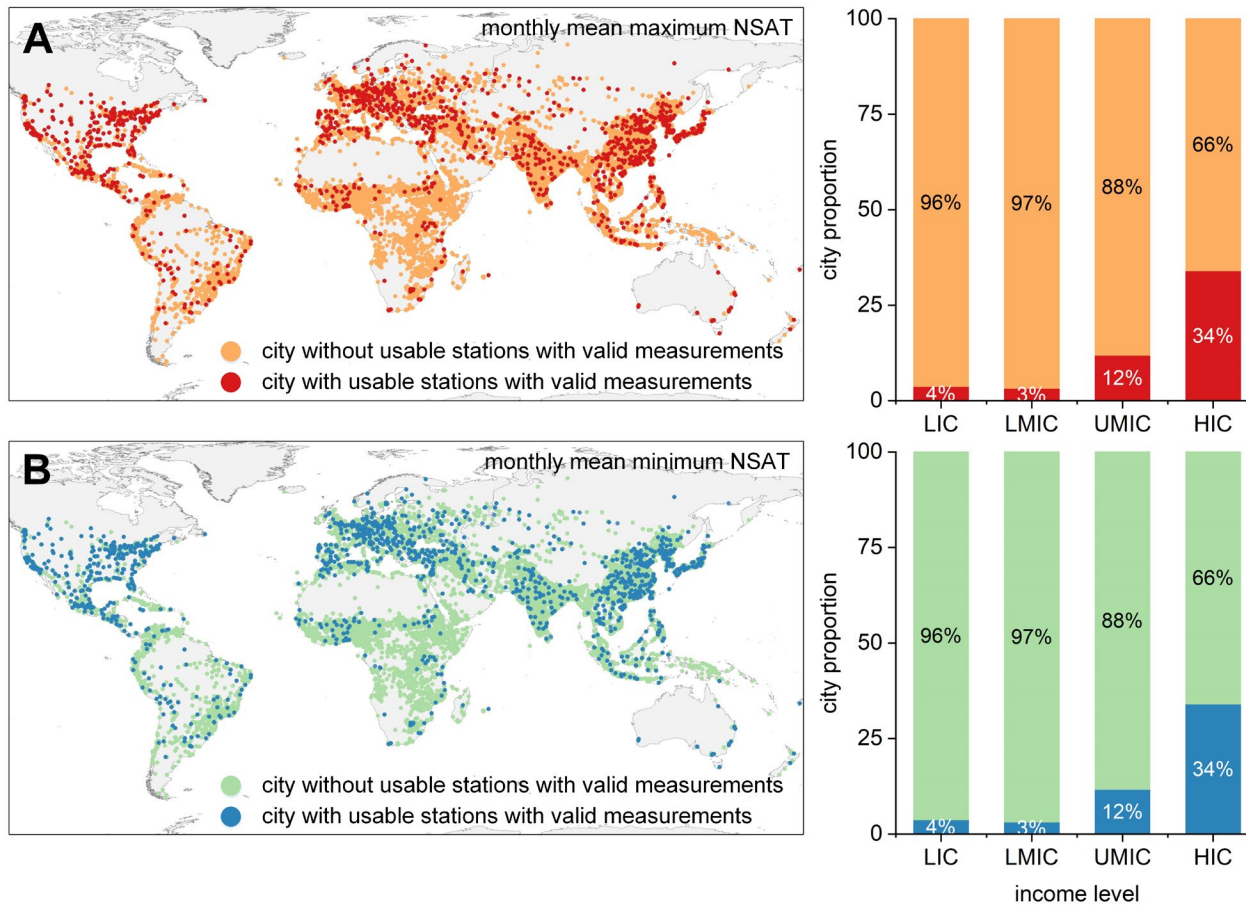


**Fig. S1. Distribution of cities with usable stations with valid measurements of monthly mean maximum and minimum near surface-air temperature (NSAT) versus those without.** (A) denotes the global distribution as well as the city proportions with and without available valid measurements for the monthly mean maximum NSAT, while (B) represents those for the monthly mean minimum NSAT. HIC, UMIC, IMIC, and LIC correspond to high-income, upper-and-middle-income, lower-and-middle-income, and low-income cities, respectively.

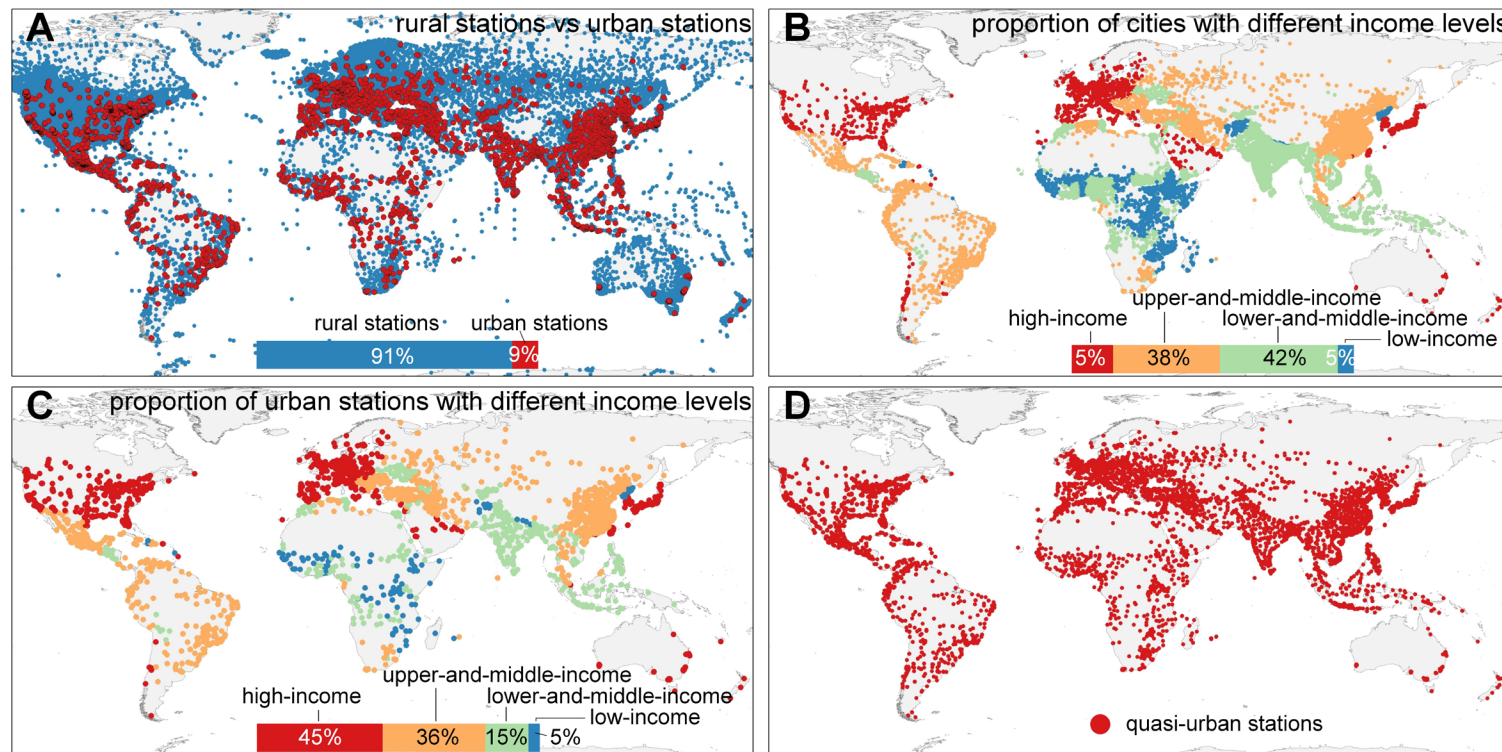


**Fig. S2. Distribution of usable weather stations and distribution of cities with different income levels.** Proportions and distribution of rural and urban stations (A); proportions and distributions of cities with different income levels (B); proportions and distribution of urban stations with different income levels (C); and distribution of quasi-urban stations within the 15-km buffer of city boundaries (D).

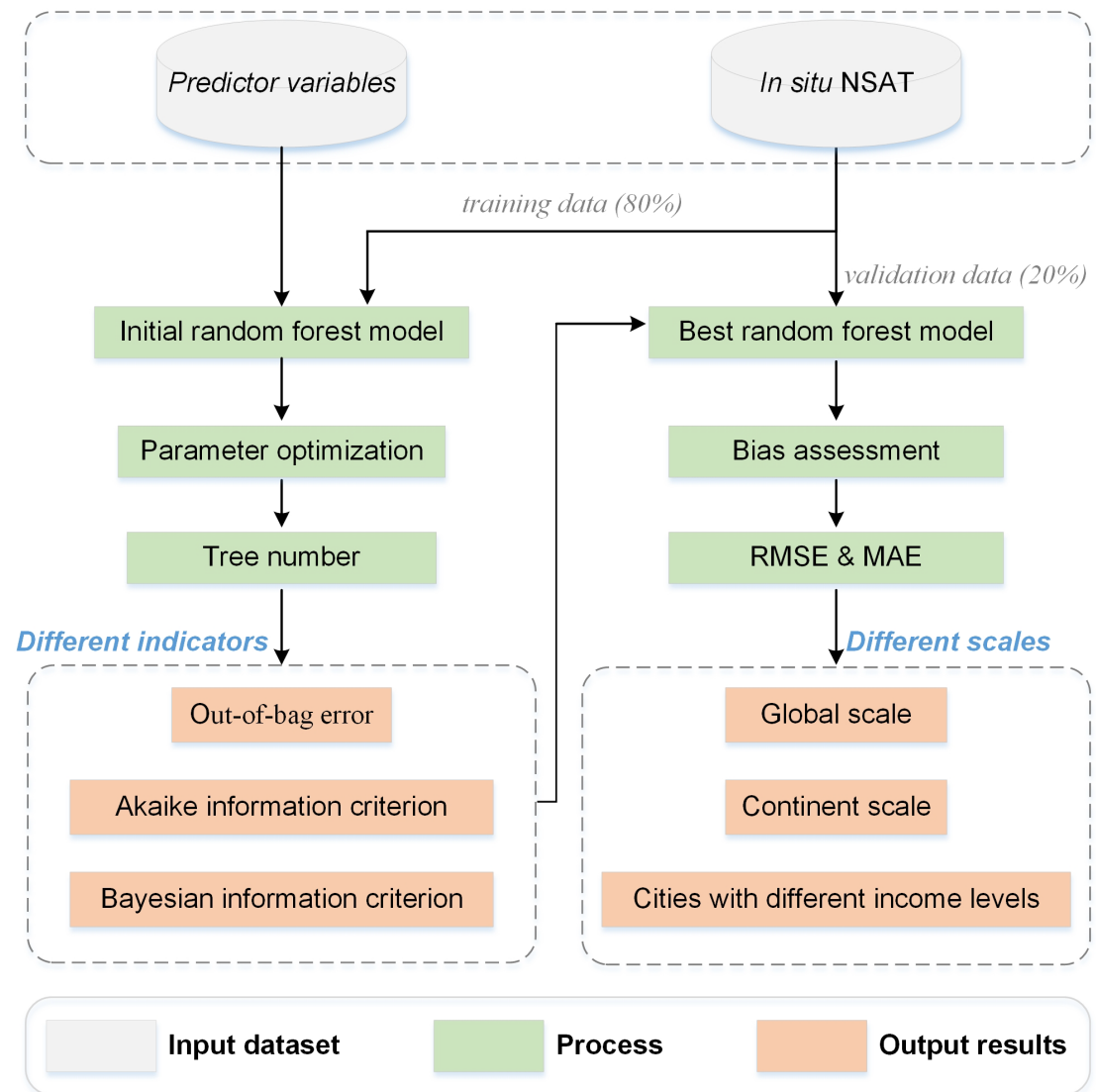


**Fig. S3. An overall schematic depicting the steps to optimize and assess the random forest model.** NSAT, RMSE, and MAE are abbreviations of the near-surface air temperature, root mean squared error, and mean absolute error, respectively.

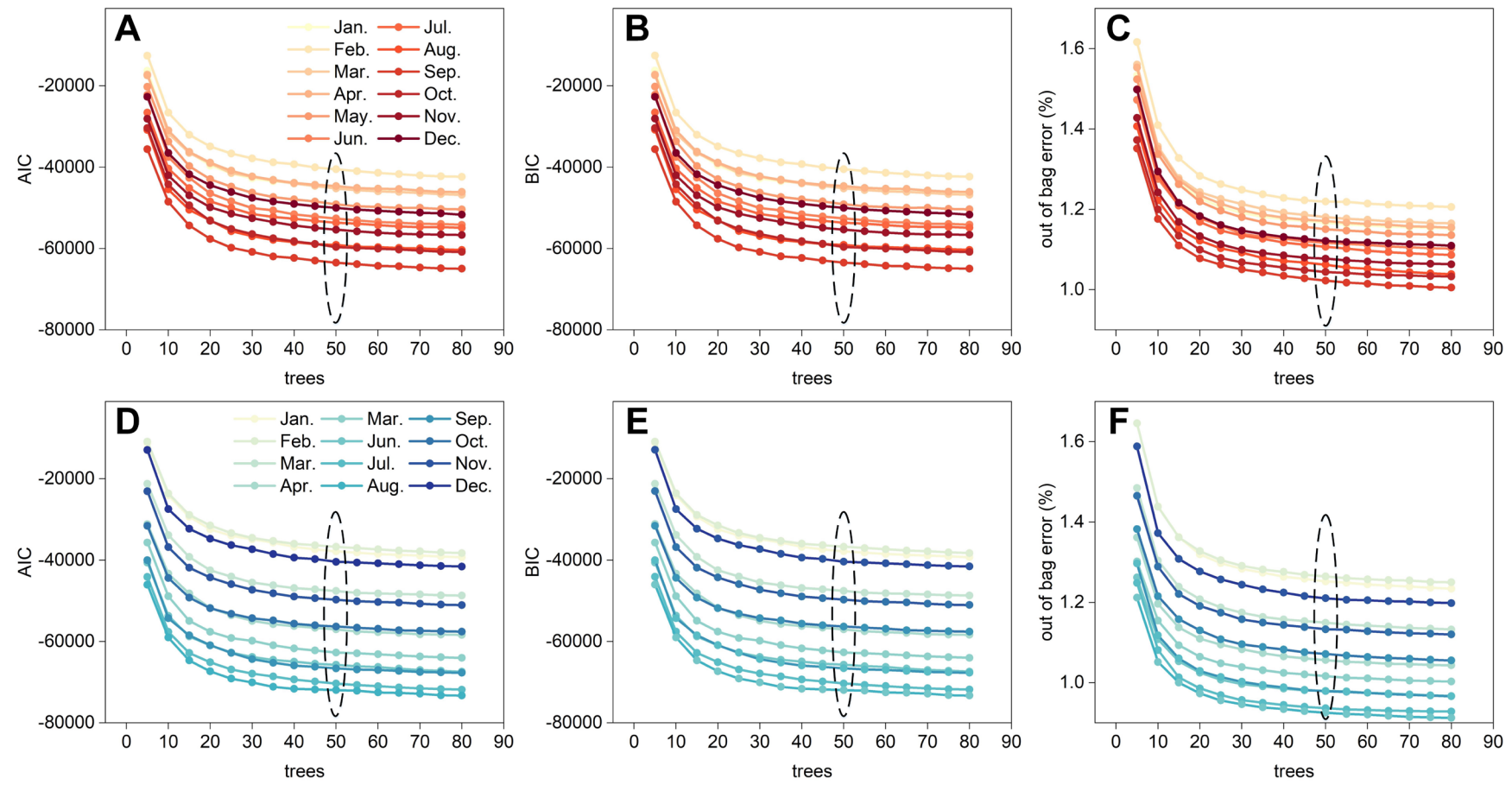


**Fig. S4. Variations of the Akaike information criterion (AIC), Bayesian Information Criterion (BIC), and out of bag error depending on tree number for each month when training the random forest model for monthly mean maximum (A, B, & C) and minimum near surface-air temperatures (D, E, & F), respectively. Once the number of trees exceeds around 50, the AIC, BIC, and out of bag errors start to converge towards a limit.**

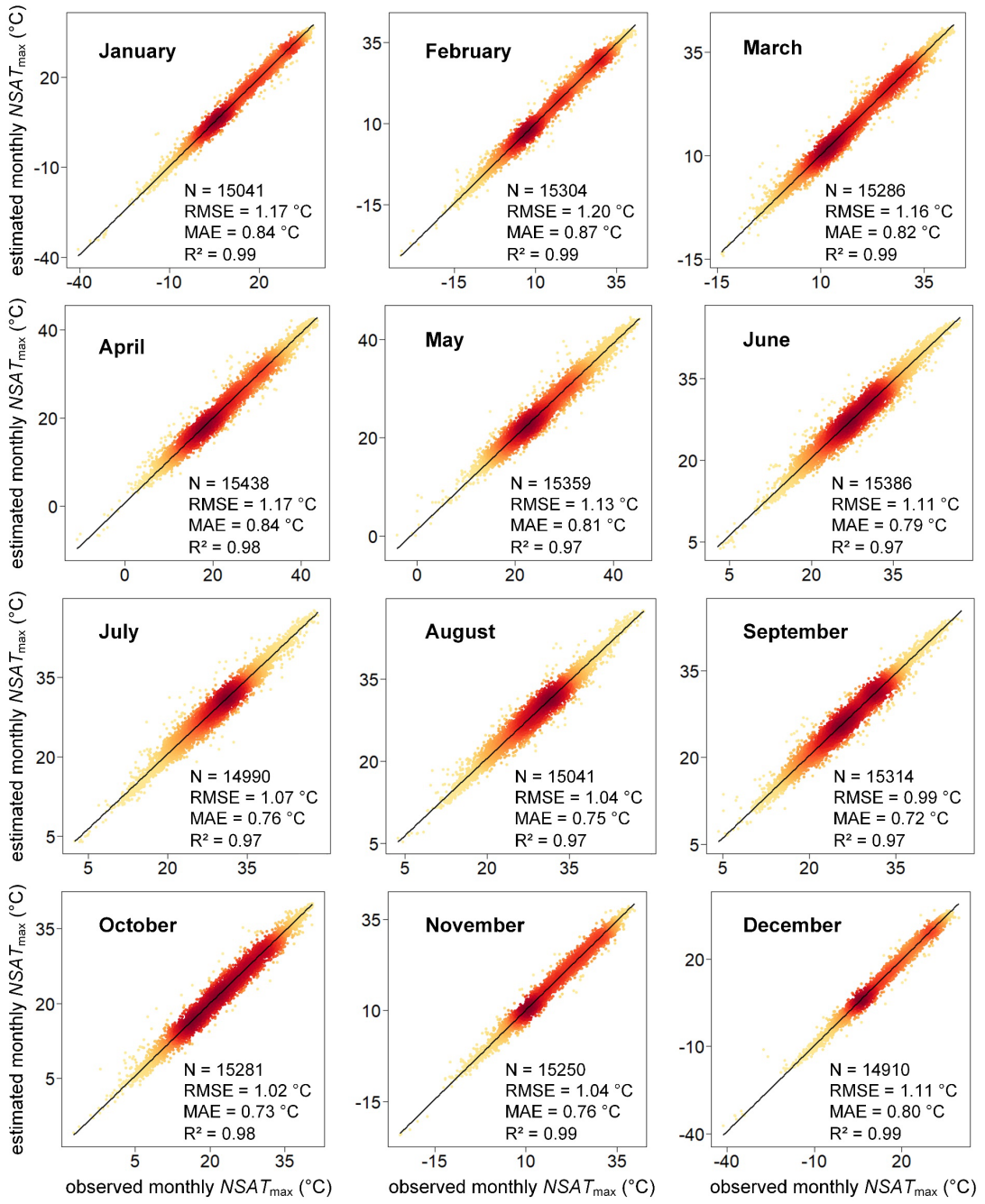


**Fig. S5. Comparisons between the observed and estimated monthly mean maximum near surface-air temperature (i.e.,  $NSAT_{max}$ ) for each month based on the global random forest model using all the temperatures as inputs.** Colors from blue to red denote the increase in point density.

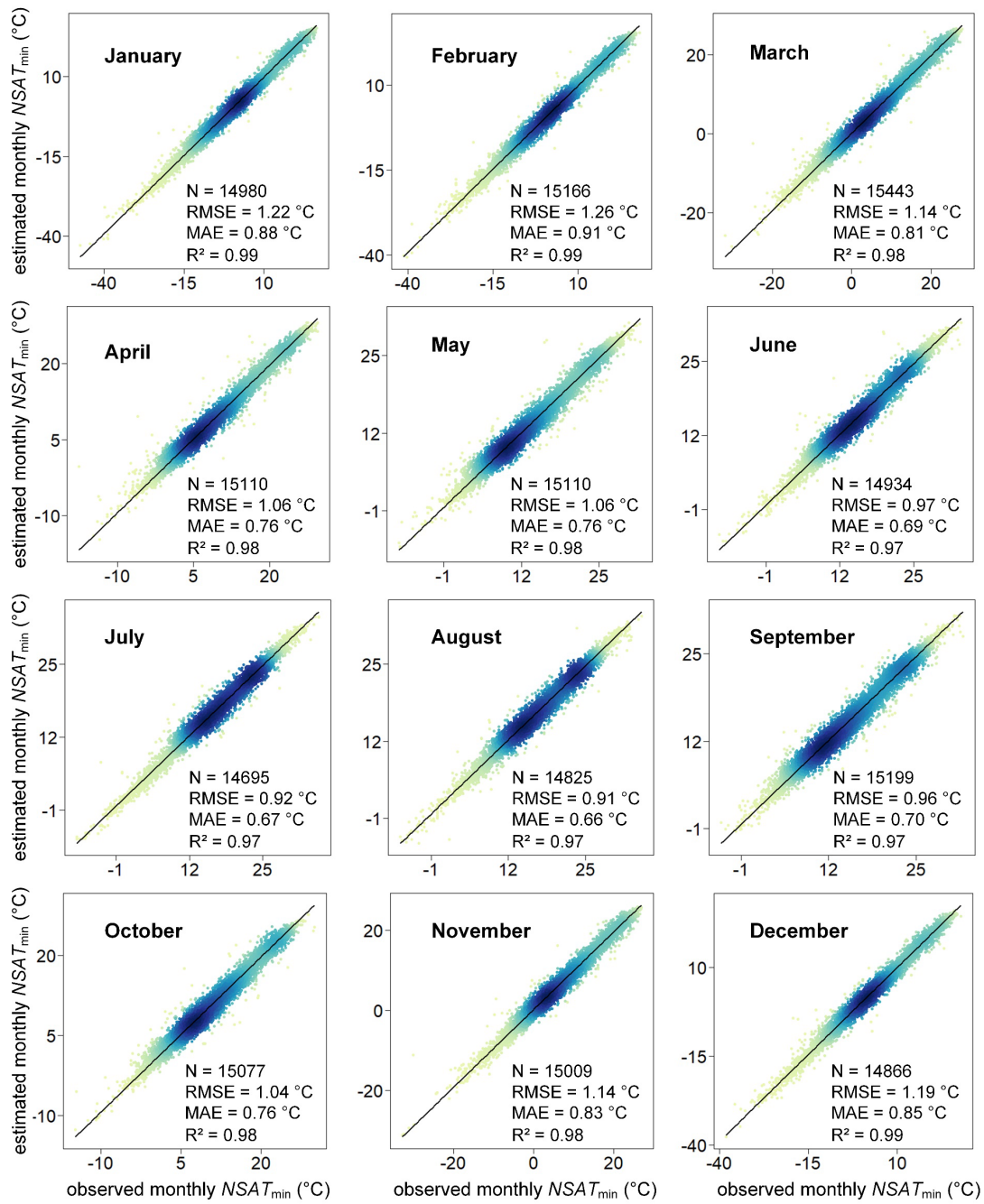


**Fig. S6. Same as Fig. S5, but for the monthly mean minimum near surface-air temperature (i.e.,  $NSAT_{min}$ ).**

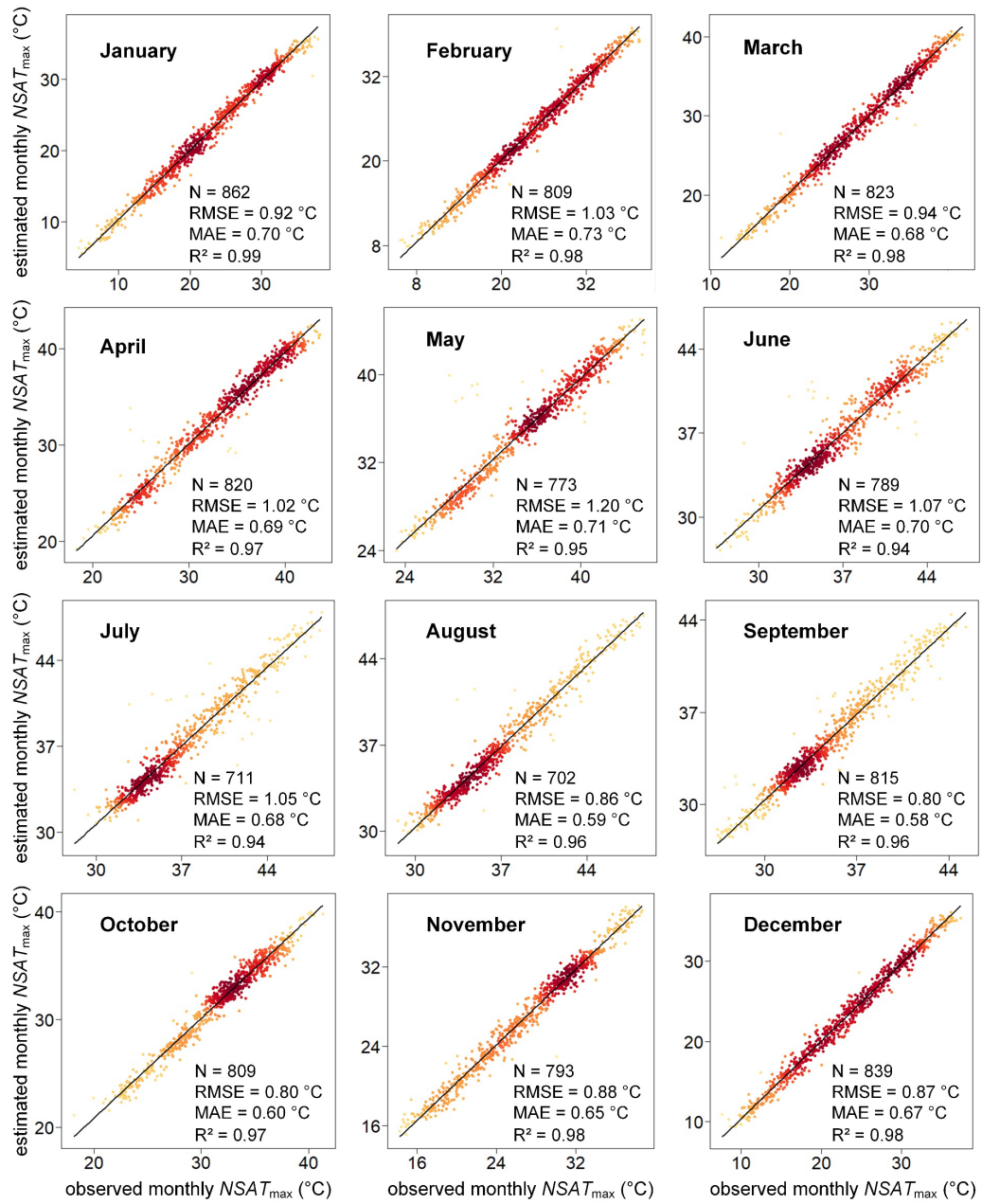


**Fig. S7. Comparisons between the observed and estimated monthly mean maximum near surface-air temperature (i.e.,  $NSAT_{max}$ ) for each month based on the local random forest model using extreme temperatures as inputs.** Colors from blue to red denote the increase in point density.

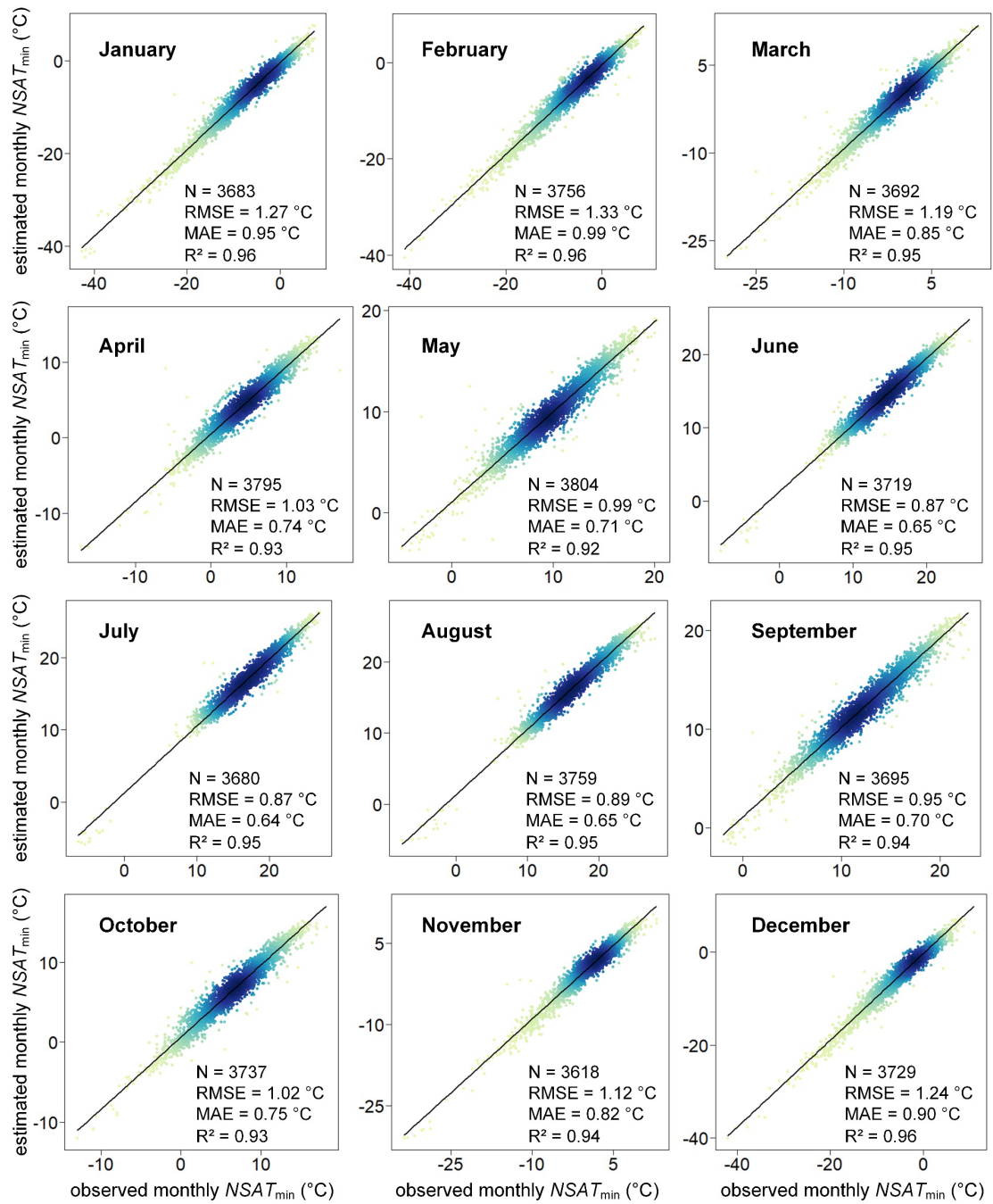


**Fig. S8.** Same as Fig. S7, but for the monthly mean minimum near surface-air temperature (i.e.,  $NSAT_{min}$ ).

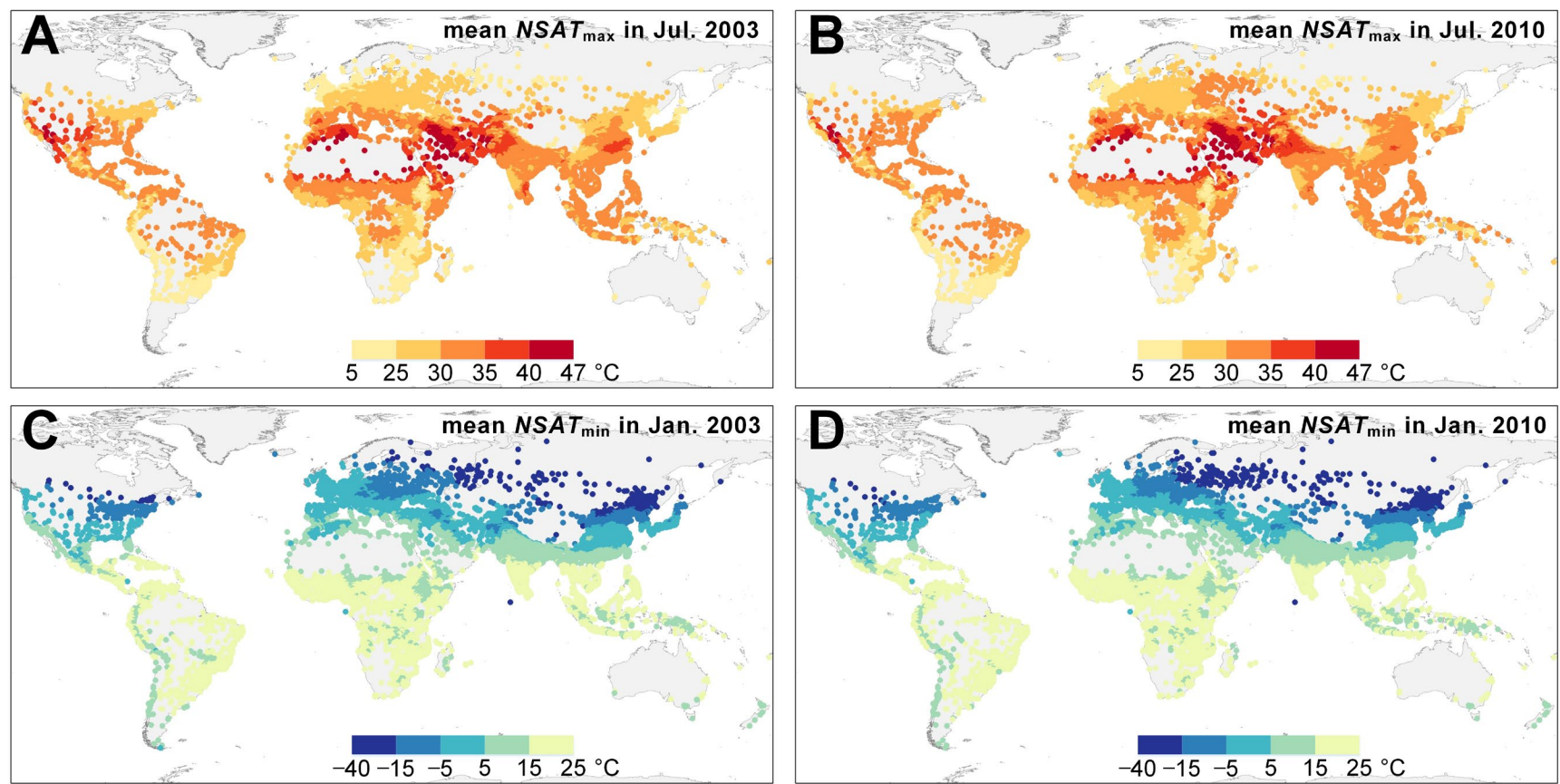


**Fig. S9. Mean maximum near surface-air temperature (i.e.,  $NSAT_{max}$ ) in Jul. 2003 (A) and 2010 (B) for each city and mean minimum near surface-air temperature (i.e.,  $NSAT_{min}$ ) in Jan. 2003 (C) and 2010 (D) for each city.**

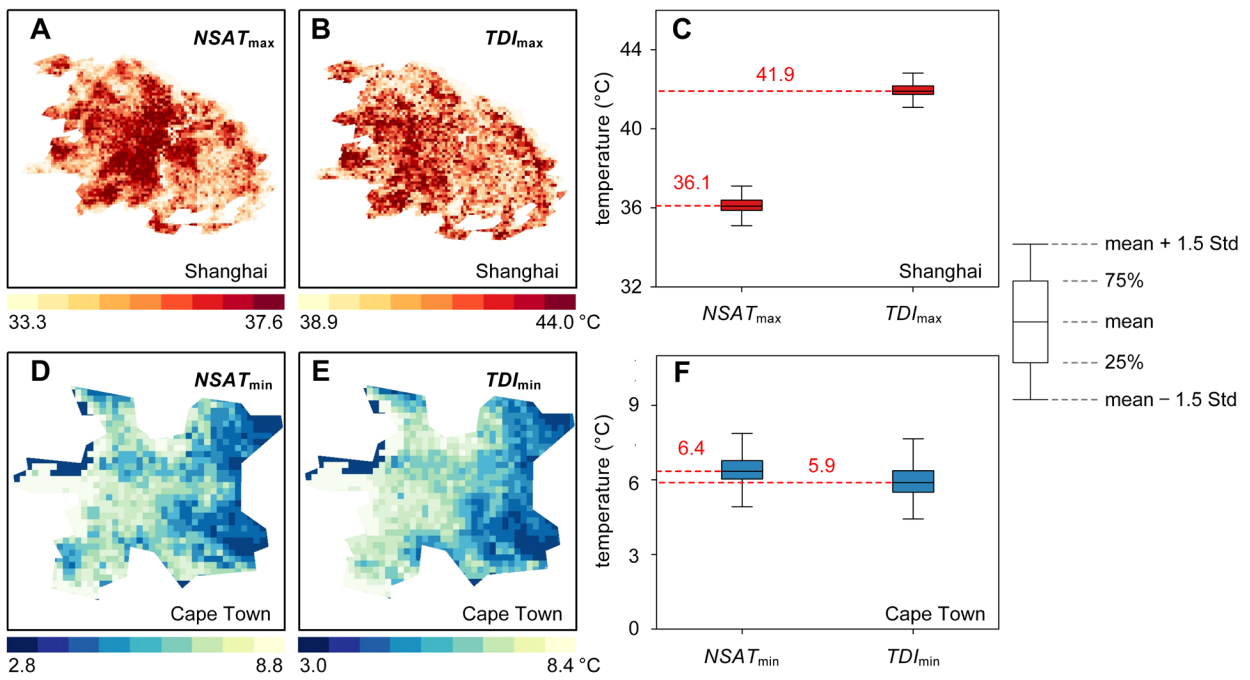


**Fig. S10. Comparison of near surface-air temperature (NSAT) and thermal discomfort index (TDI) over Shanghai of China and Cape Town of South Africa.** The Shanghai case (A, B, & C) and the Cape Town case (D, E, & F); and statistical distributions of pixel-based temperature values for Shanghai (C) and Cape Town (F), respectively.

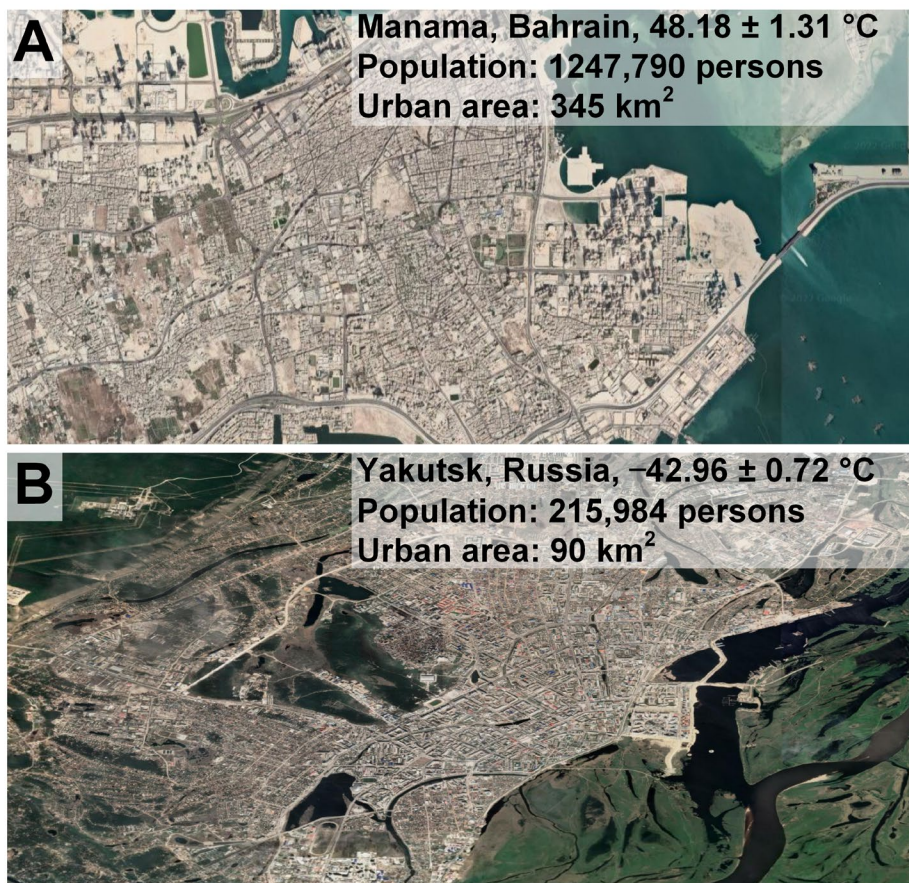


**Fig. S11. High-resolution satellite-derived images of the identified world's hottest city (Manama, A) and the coldest city (Yakutsk, B).**

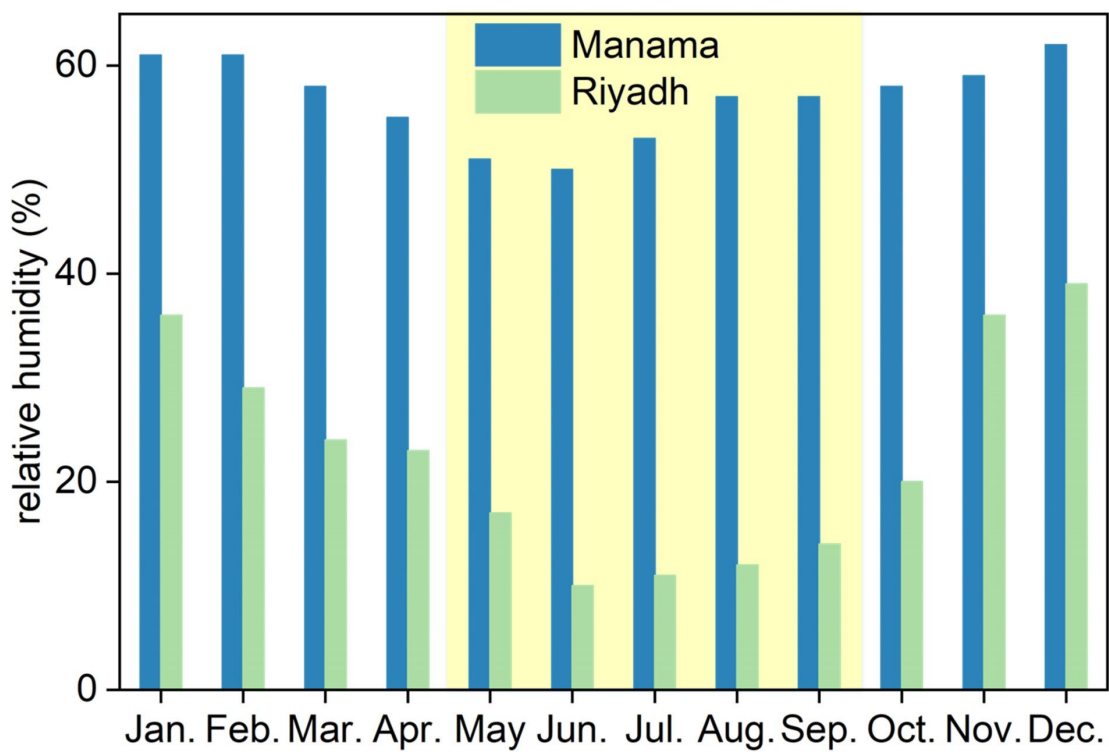


**Fig. S12. Comparison of monthly mean relative humidity between Manama in Bahrain and Riyadh in Saudi Arabia (refer to <https://www.worldweatheronline.com>).** The background light yellow denotes the hot months.

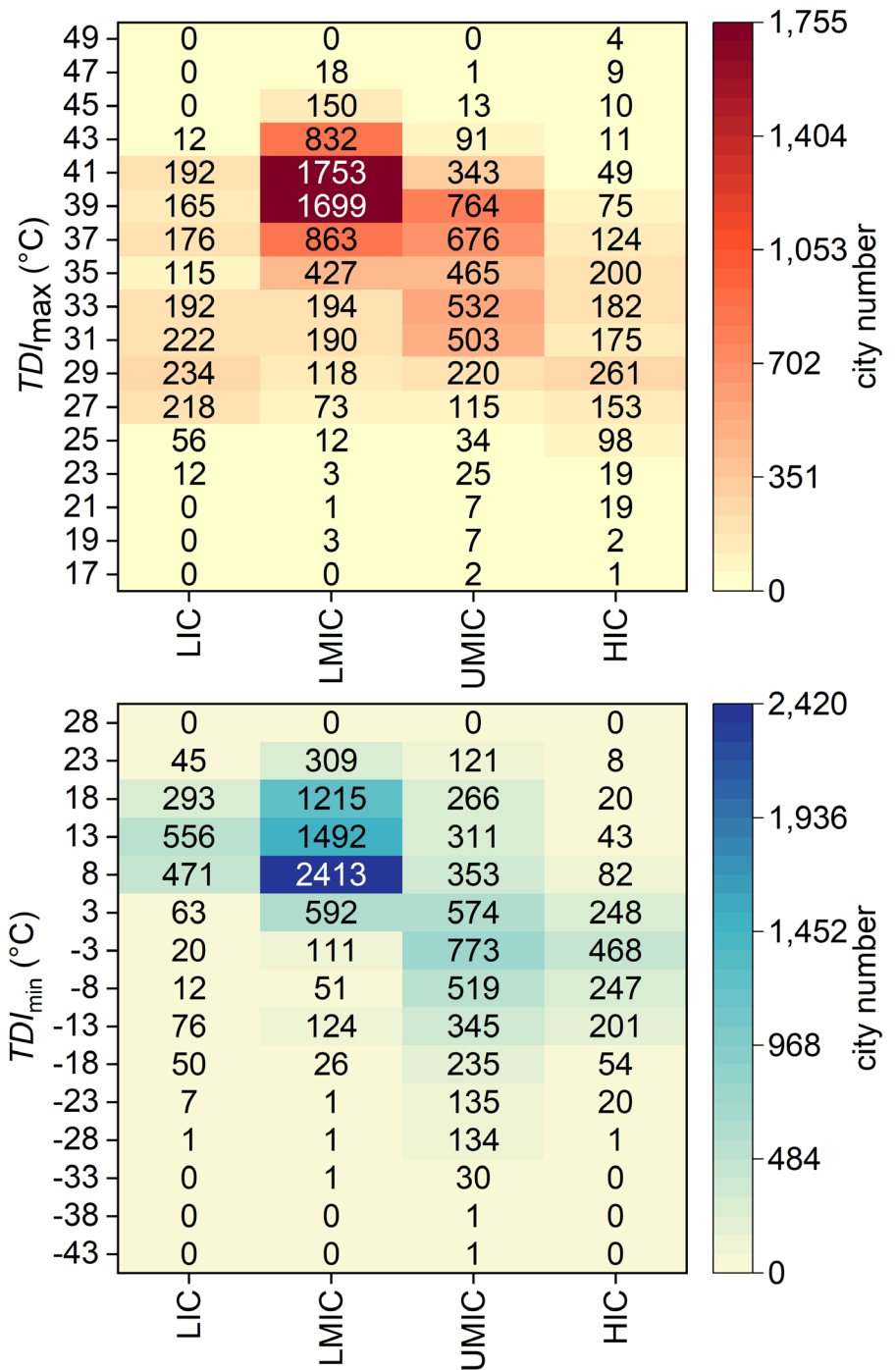


**Fig. S13. The number of  $TDI_{max}$  and  $TDI_{min}$  cities under different income levels.** LIC, LMIC, UMIC, and HIC represent the low-income, lower-and-middle-income, upper-and-middle-income, and high-income cities, respectively.

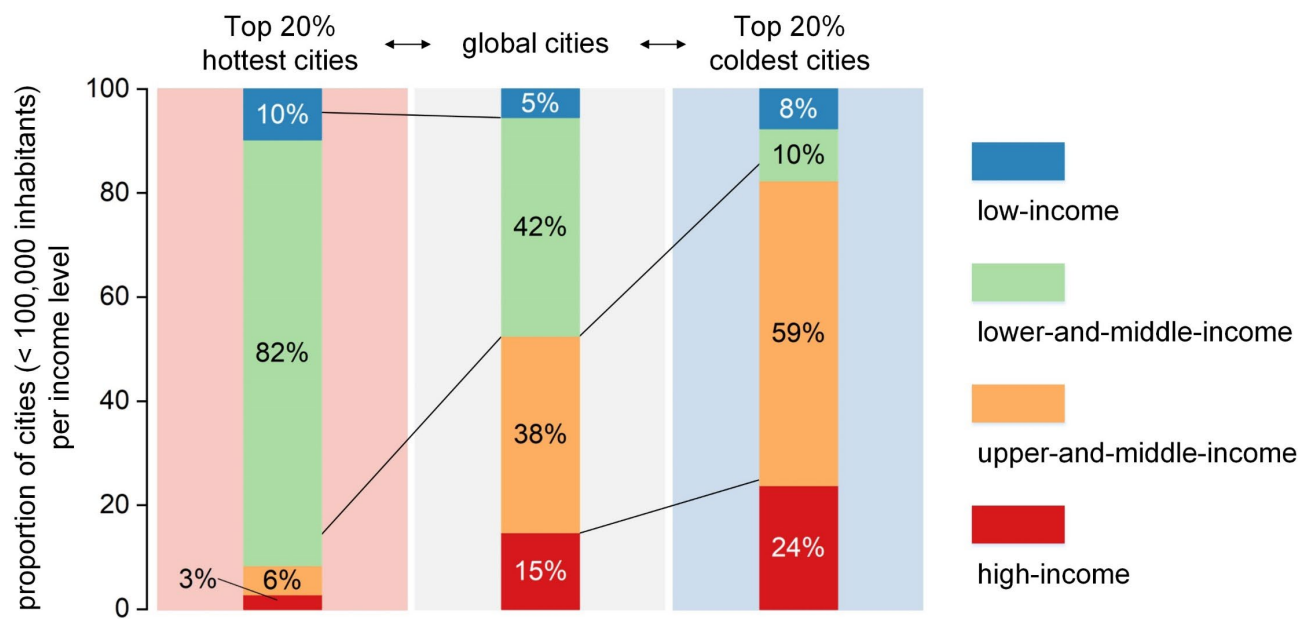


**Fig. S14. Proportions of Top 20% hottest and coldest cities with a population < 100,000 at different income levels.**

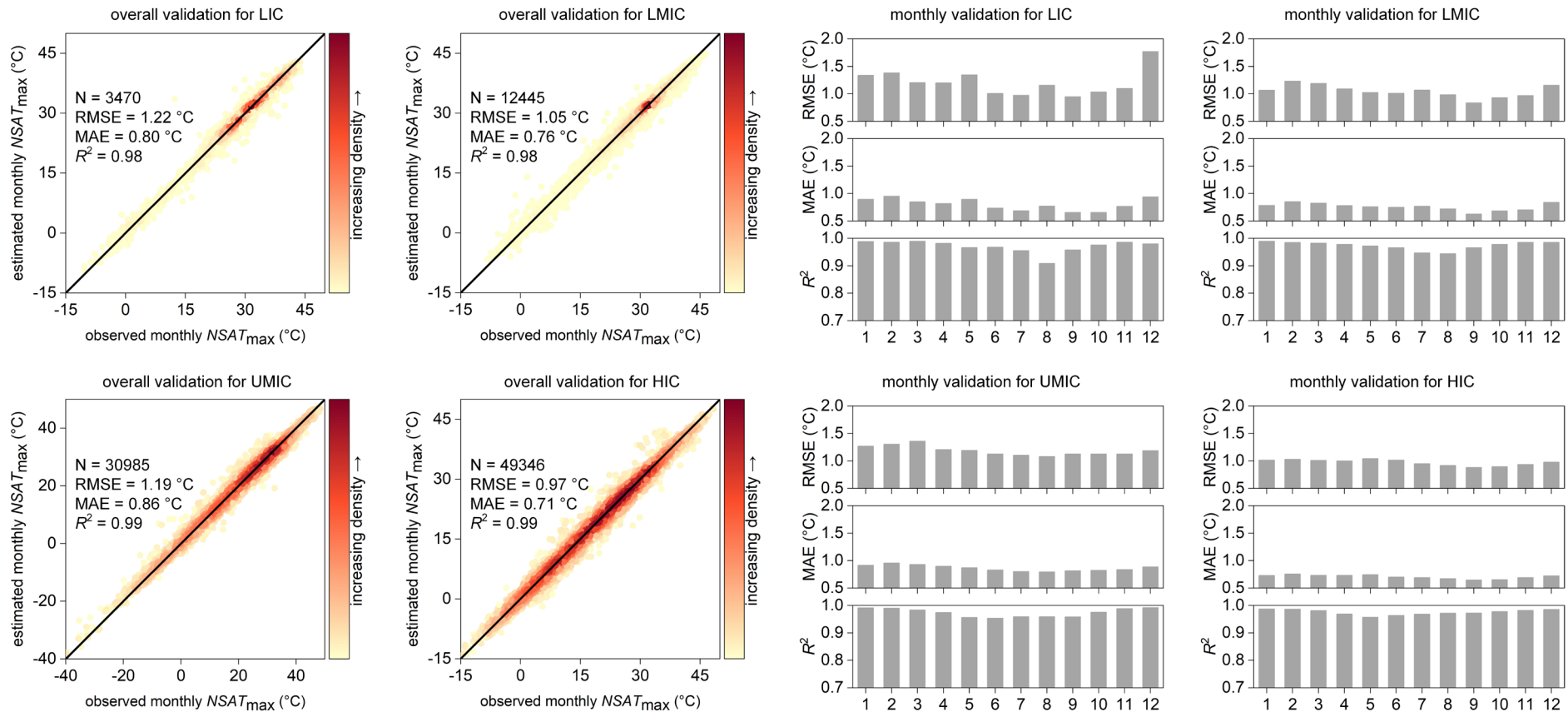


**Fig. S15. Overall and monthly validations for the monthly mean maximum near surface-air temperature (i.e.,  $NSAT_{max}$ ) across cities with different income levels.** LIC, LMIC, UMIC, and HIC correspond to the cities of low-income, lower-and-middle-income, upper-and-middle-income, and high-income, respectively.

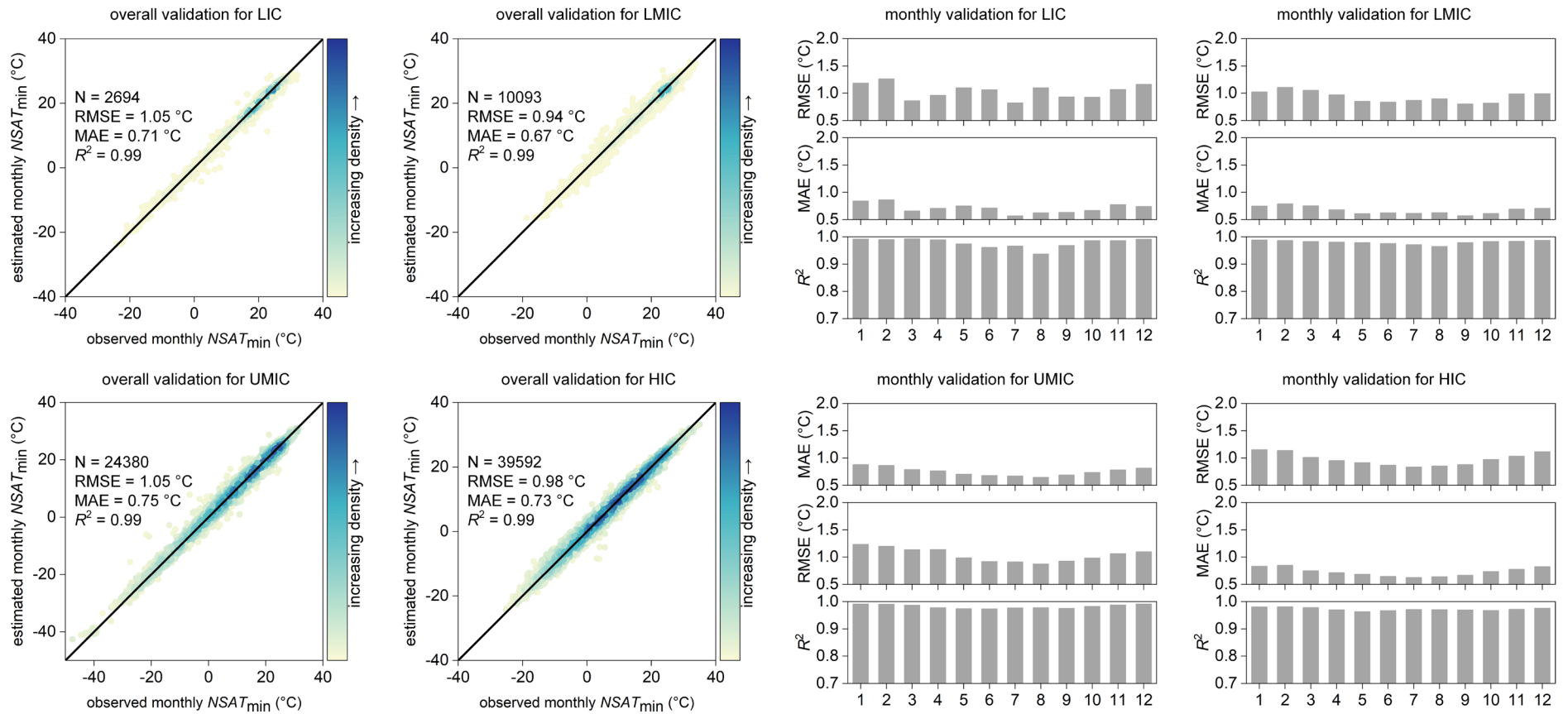


**Fig. S16.** Same as Fig. S15, but for the monthly mean minimum near surface-air temperature (i.e.,  $NSAT_{min}$ ).

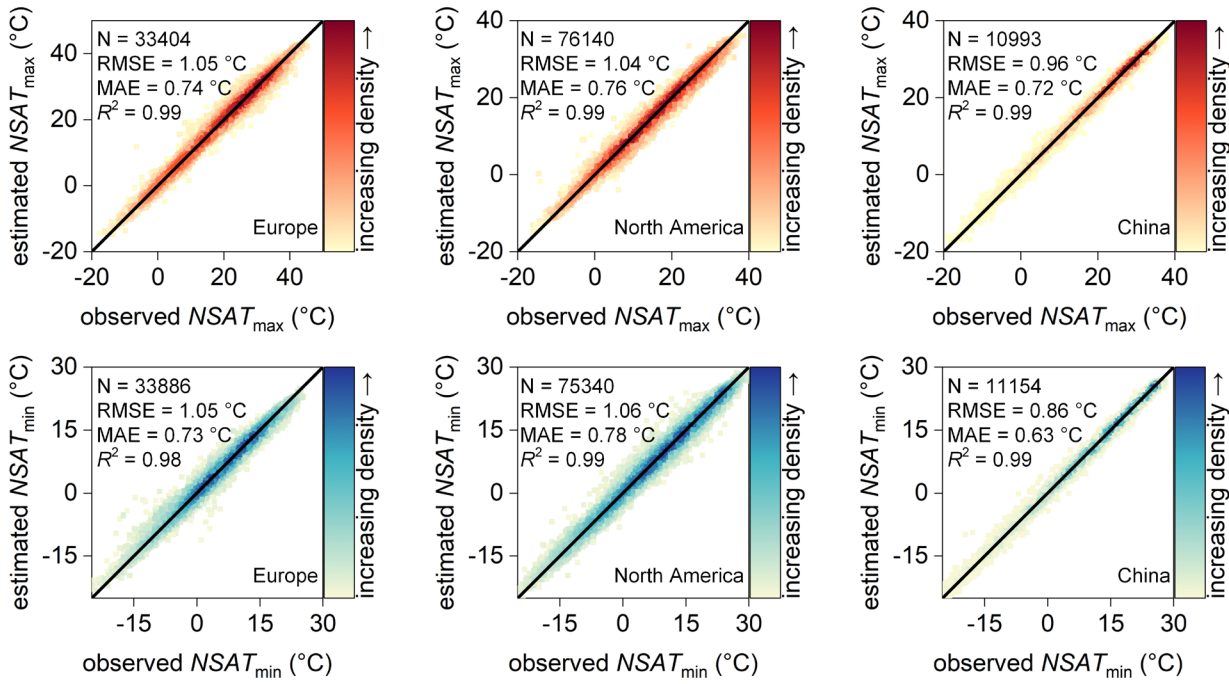


**Fig. S17. Overall validations for the monthly mean maximum and minimum near surface-air temperatures (i.e.,  $NSAT_{max}$  and  $NSAT_{min}$ ) over Europe, North America, and China.**

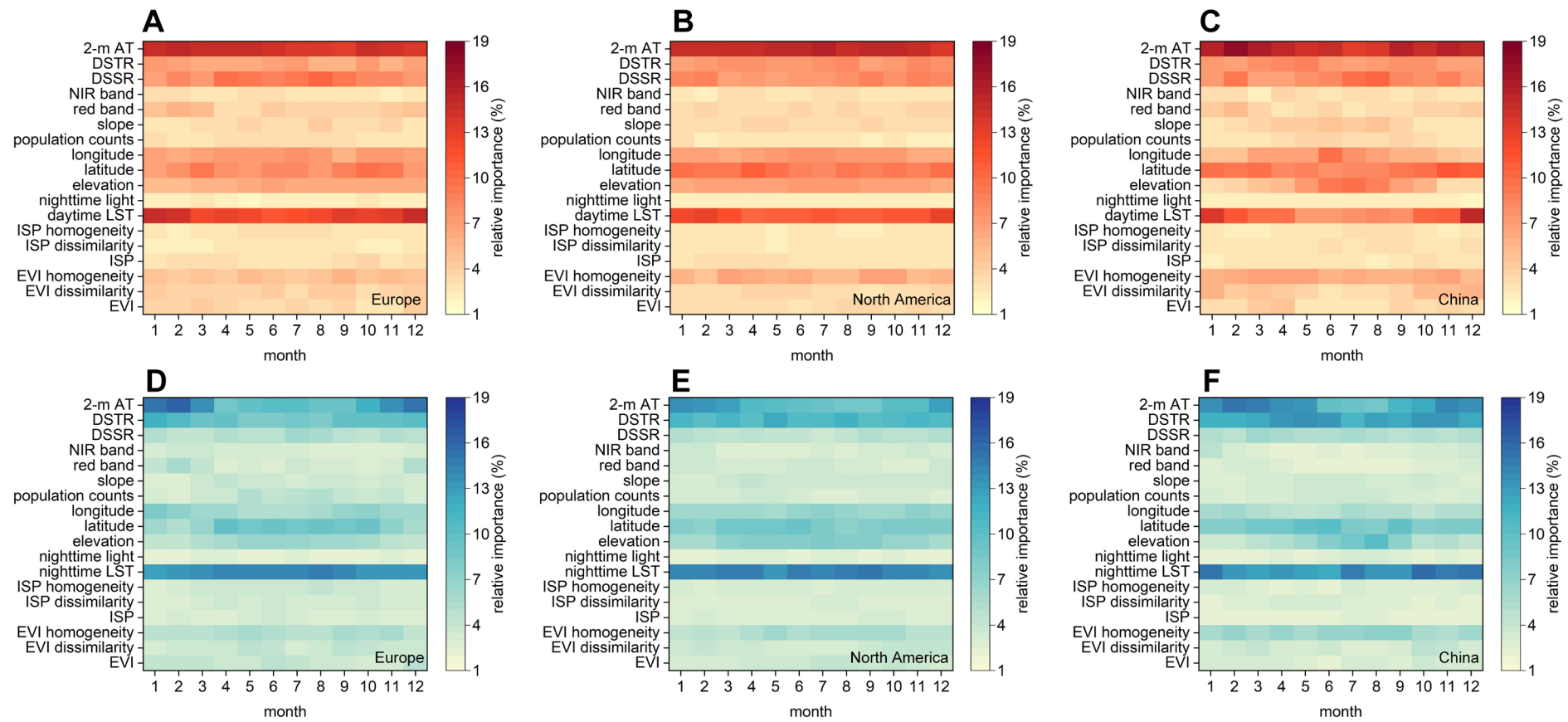


**Fig. S18. Monthly relative importance of input variables for random forest models over Europe, North America, and China.** Relative importance scores (in %) of input variables for the models of monthly mean maximum (A, B, and C) and minimum (D, E, and F) near surface-air temperatures, respectively. The 2-m AT, DSTR, DSSR, NIR band, red band, LST, ISP, and EVI represent 2-m air temperature, downward surface thermal radiation, downward surface solar radiation, surface reflectance for the near-infrared band, surface reflectance for the red band, land surface temperature, impervious surface percentage, and enhanced vegetation index, respectively.

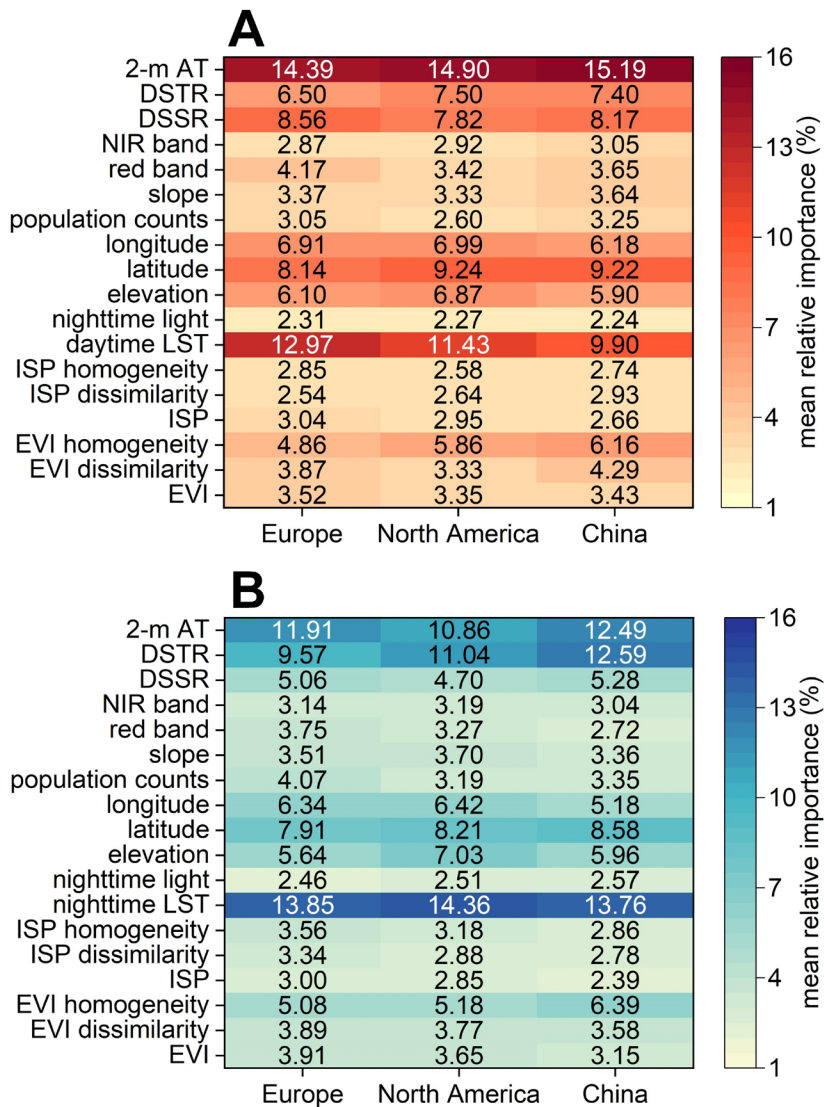


**Fig. S19. Mean relative importance of input variables for random forest models over Europe, North America, and China.** Relative importance scores (in %) of input variables for the models of monthly mean maximum (A) and minimum (B) near surface-air temperatures, respectively. The 2-m AT, DSTR, DSSR, NIR band, red band, LST, ISP, and EVI represent 2-m air temperature, downward surface thermal radiation, downward surface solar radiation, surface reflectance for the near-infrared band, surface reflectance for the red band, land surface temperature, impervious surface percentage, and enhanced vegetation index, respectively.

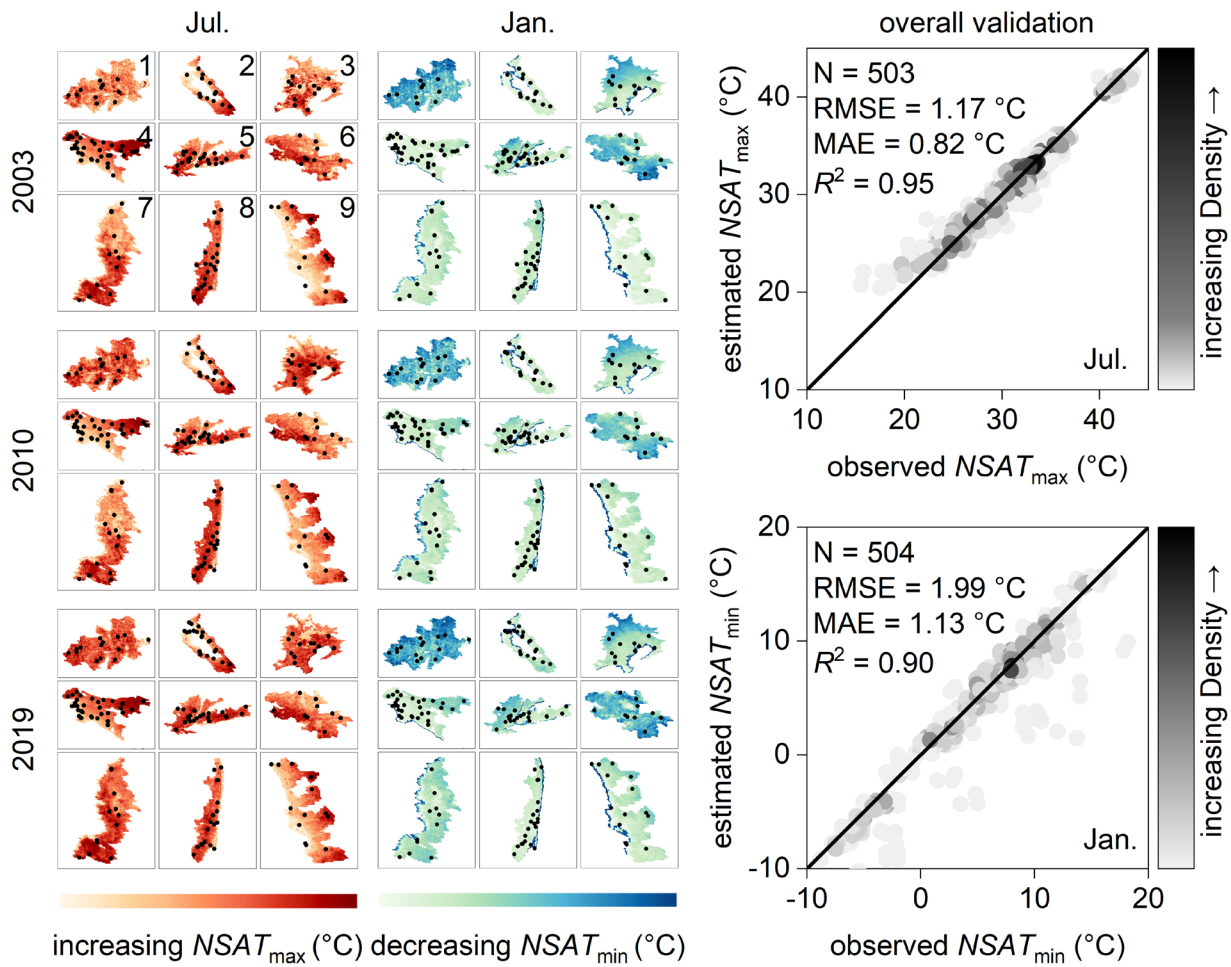


**Fig. S20. Validation for the intra-urban variability of monthly mean maximum and minimum near surface-air temperatures (i.e.,  $NSAT_{max}$  and  $NSAT_{min}$ ) across nine cities with relatively dense weather stations.** The numbers from 1 to 9 refer to Dallas-Fort Worth, San Francisco-Oakland, Tokyo, Los Angeles-Long Beach-Santa Ana, New York-Newark, Phoenix-Mesa, Seattle, Miami, and San Diego, respectively.

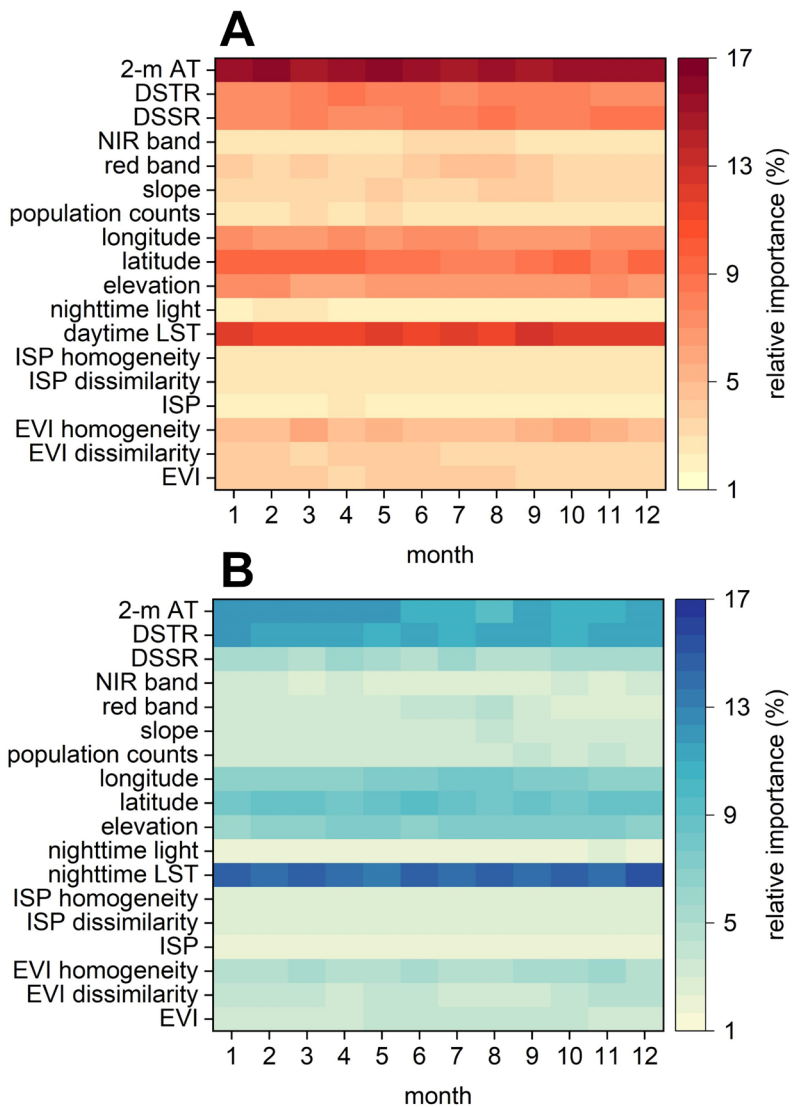


**Fig. S21. Relative importance of input variables for random forest models in estimating monthly mean maximum (A) and minimum (B) near surface-air temperatures.** The 2-m AT, DSTR, DSSR, NIR band, red band, LST, ISP, and EVI denote 2-m air temperature, downward surface thermal radiation, downward surface solar radiation, surface reflectance for the near-infrared band, surface reflectance for the red band, land surface temperature, impervious surface percentage, and enhanced vegetation index, respectively.

**Table S1. Monthly numbers of valid samples for the global random forest models using all the temperatures as inputs.**

<b>month</b>	<b><math>NSAT_{max}</math></b>	<b><math>NSAT_{min}</math></b>	<b>month</b>	<b><math>NSAT_{max}</math></b>	<b><math>NSAT_{min}</math></b>
January	81,555	81,047	July	81,122	80,174
February	81,758	81,351	August	81,407	80,520
March	82,124	81,613	September	81,763	80,850
April	81,756	81,347	October	81,700	81,033
May	81,761	81,050	November	81,180	80,823
June	81,733	80,877	December	80,768	80,268

**Table S2.** Input variables used to train the random forest models to predict NSAT and TDI.

Variable type	Variable order	Variable name	Descriptions	Temporal resolution	Spatial resolution
land surface	1	daytime LST (K)	1:30 pm during the day, derived from MODIS data	monthly	1 km
temperature (LST)	2	nighttime LST (K)	1:30 am at night, derived from MODIS data	monthly	1 km
	3	impervious surface percentage (%)	estimated percentage of impervious surface areas in each 90×90 m <sup>2</sup> grid, derived from the GAIA dataset	yearly	90 m
	4	population counts (person)	estimated residential population in each 90×90 m <sup>2</sup> grid, derived from the Annual 90-m WorldPop Global Project	yearly	90 m
auxiliary variable			Population Data		
	5	nighttime light	derived from the annual 1-km harmonization of DMSP and VIIRS nighttime light data	yearly	1 km
	6	elevation (m)	digital surface model (DSM), derived from the 30-m ALOS Global Digital Surface Model	/	30 m

7	slope (°)	DSM-derived slope, derived from the 30-m ALOS Global Digital Surface Model	/	30 m
8	longitude (°)	DSM-derived longitude, derived from the 30-m ALOS Global Digital Surface Model	/	30 m
9	latitude (°)	DSM-derived latitude, derived from the 30-m ALOS Global Digital Surface Model	/	30 m
10	spectral reflectance	surface reflectance for MODIS bands 1 & 2, derived from MODIS data	monthly	500 m
11	enhanced vegetation index	derived from MODIS data	monthly	250 m
12	dissimilarity of impervious surface percentage	derived from gray level co-occurrence matrix of impervious surface percentage	yearly	1 km
13	homogeneity of impervious surface percentage	derived from gray level co-occurrence matrix of impervious surface percentage	yearly	1 km
14	dissimilarity of enhanced vegetation index	derived from gray level co-occurrence matrix of enhanced vegetation index	yearly	1 km

15	homogeneity of enhanced vegetation index	derived from gray level co-occurrence matrix of enhanced vegetation index	yearly	1 km
16	2-m air temperature (°C)	derived from ERA5-Land reanalysis data	monthly	resampled 1 km
17	downward surface solar radiation (J/m <sup>2</sup> )	derived from ERA5-Land reanalysis data	monthly	resampled 1 km
18	downward surface thermal radiation (J/m <sup>2</sup> )	derived from ERA5-Land reanalysis data	monthly	resampled 1 km

**Table S3. Number of valid samples of each year from quasi-urban sites.**

<b>year</b>	<b><i>NSAT</i><sub>max</sub></b>	<b><i>NSAT</i><sub>min</sub></b>	<b>year</b>	<b><i>NSAT</i><sub>max</sub></b>	<b><i>NSAT</i><sub>min</sub></b>
2003	54,866	54,185	2012	60,010	59,556
2004	55,649	55,157	2013	57,500	57,125
2005	58,028	57,733	2014	57,459	56,734
2006	57,780	57,489	2015	56,577	55,969
2007	58,137	57,618	2016	56,546	56,256
2008	59,507	58,808	2017	56,644	56,347
2009	60,041	59,494	2018	54,341	54,107
2010	60,471	59,877	2019	54,258	54,165
2011	60,813	60,333			

**Table S4. Monthly numbers of valid samples for the local random forest models using extreme temperatures as inputs.**

month	$NSAT_{max}$	$NSAT_{min}$	month	$NSAT_{max}$	$NSAT_{min}$
January	4,090	19,189	July	4,141	18,929
February	4,110	19,234	August	4,176	19,079
March	4,095	19,307	September	4,163	19,144
April	4,067	19,228	October	4,106	19,229
May	4,129	19,109	November	4,103	19,205
June	4,148	19,054	December	4,107	19,191

**Table S5.** The world's Top 10 hottest cities with urban built-up area > 10 km<sup>2</sup>.

Ranking	City	Climate	Country	Area (km <sup>2</sup> )	Population (person)	T <sub>max</sub> ± std (°C)
1	<b>Manama</b>	arid	Bahrain	345	1247,790	48.18 ± 1.31
2	<b>Ras Laffan</b>	arid	Qatar	26	74,199	47.86 ± 0.86
3	<b>Al Qunfudhah</b>	arid	Saudi Arabia	10	96,487	47.80 ± 1.75
4	<b>Shahdadkot</b>	arid	Pakistan	11	213,098	47.17 ± 0.80
5	<b>Al-Hawr</b>	arid	Qatar	13	52,366	47.11 ± 0.73
6	<b>Usta Muhammad</b>	arid	Pakistan	12	137,181	47.01 ± 0.85
7	<b>Thuqbah</b>	arid	Saudi Arabia	134	364,257	46.96 ± 1.06
8	<b>Ar-Rayyan</b>	arid	Qatar	380	1556,520	46.67 ± 0.98
9	<b>Leiah</b>	arid	Pakistan	30	82,987	46.60 ± 0.70
10	<b>Munda</b>	arid	Pakistan	27	99,986	46.35 ± 0.69

**Table S6.** The world's Top 10 coldest cities with urban built-up area > 10 km<sup>2</sup>.

Ranking	City	Climate	Country	Area (km <sup>2</sup> )	Population (person)	T <sub>min</sub> ± std (°C)
1	<b>Yakutsk</b>	snow	Russia	90	215,984	-42.96 ±0.72
2	<b>Novy Urengoy</b>	snow	Russia	36	96,123	-36.99 ±0.93
3	<b>Norilsk</b>	snow	Russia	23	69,024	-36.82 ±0.72
4	<b>Nizhnevartovsk</b>	snow	Russia	45	123,163	-35.12 ±0.62
5	<b>Kyzyl</b>	semi-arid	Russia	26	84,273	-33.85 ±0.80
6	<b>Yakeshi</b>	snow	China	24	132,936	-32.42 ±0.60
7	<b>Haila'Er</b>	snow	China	47	209,890	-31.97 ±0.88
8	<b>Nenjiang</b>	snow	China	25	140,203	-31.89 ±0.51
9	<b>Tomsk</b>	snow	Russia	143	529,132	-31.55 ±0.93
10	<b>Chita</b>	snow	Russia	59	184,185	-31.35 ±1.34

## REFERENCES

- Balsamo, G., A. Beljaars, K. Scipal, P. Viterbo, B. van den Hurk, M. Hirschi, and A. K. Betts, 2009: A revised hydrology for the ECMWF model: Verification from field site to terrestrial water storage and impact in the Integrated Forecast System. *J. Hydrometeorol.*, **10**, 623–643, <https://doi.org/10.1175/2008JHM1068.1>.
- Bassett, R., V. Janes-Bassett, J. Phillipson, P. J. Young, and G. S. Blair, 2021: Climate driven trends in London's urban heat island intensity reconstructed over 70 years using a generalized additive model. *Urban Clim.*, **40**, 100990, <https://doi.org/10.1016/j.uclim.2021.100990>.
- Chakraborty, T., and X. Lee, 2019: A simplified urban-extent algorithm to characterize surface urban heat islands on a global scale and examine vegetation control on their spatiotemporal variability. *Int. J. Appl. Earth Obs. Geoinf.*, **74**, 269–280, <https://doi.org/10.1016/j.jag.2018.09.015>.
- Chakraborty, T., Z. S. Venter, Y. Qian, and X. Lee, 2022: Lower Urban Humidity Moderates Outdoor Heat Stress. *AGU Adv.*, **3**, e2022AV000729, <https://doi.org/10.1029/2022AV000729>.
- Clemens, K. K., A. M. Ouédraogo, L. Li, J. A. Voogt, J. Gilliland, E. S. Krayenhoff, S. Leroyer, and S. Z. Shariff, 2021: Evaluating the association between extreme heat and mortality in urban Southwestern Ontario using different temperature data sources. *Sci. Rep.*, **11**, 1–11, <https://doi.org/10.1038/s41598-021-87203-0>.
- Clinton, N., and P. Gong, 2013: MODIS detected surface urban heat islands and sinks: Global locations and controls. *Remote Sens. Environ.*, **134**, 294–304, <https://doi.org/10.1016/j.rse.2013.03.008>.
- dos Santos, R. S., 2020: Estimating spatio-temporal air temperature in London (UK) using machine learning and earth observation satellite data. *Int. J. Appl. Earth Obs. Geoinf.*, **88**, 102066, <https://doi.org/10.1016/j.jag.2020.102066>.
- Du, R. J., Song, X. Huang, Q. Wang, C. Zhang, O. Brousse, P. and W. Chan, 2022: High-resolution regional modeling of urban moisture island: mechanisms and implications on

- thermal comfort. *Build. Environ.*, **207**, 108542, <https://doi.org/10.1016/j.buildenv.2021.108542>.
- Ho, H. C., A. Knudby, P. Sirovyak, Y. Xu, M. Hodul, and S. B. Henderson, 2014: Mapping maximum urban air temperature on hot summer days. *Remote Sens. Environ.*, **154**, 38–45, <https://doi.org/10.1016/j.rse.2014.08.012>.
- Hooker, J., G. Duveiller, and A. Cescatti, 2018: A global dataset of air temperature derived from satellite remote sensing and weather stations. *Sci. Data*, **5**, 1–11, <https://doi.org/10.1038/sdata.2018.246>.
- Huang, J., J. G. Cedeño-Laurent, and J. D. Spengler, 2014: CityComfort+: A simulation-based method for predicting mean radiant temperature in dense urban areas. *Build. Environ.*, **80**, 84–95, <https://doi.org/10.1016/j.buildenv.2014.05.019>.
- Jiang, L., W. Zhan, L. Hu, F. Huang, F. Hong, Z. Liu, J. Lai, and C. Wang, 2021: Assessment of different kernel-driven models for daytime urban thermal radiation directionality simulation. *Remote Sens. Environ.*, **263**, 112562, <https://doi.org/10.1016/j.rse.2021.112562>.
- Lindberg, F., B. Holmer, and S. Thorsson, 2008: SOLWEIG 1.0 – Modelling spatial variations of 3D radiant fluxes and mean radiant temperature in complex urban settings. *Int. J. Biometeorol.*, **52**, 697–713, <https://doi.org/10.1007/s00484-008-0162-7>.
- Luo, Z., J. Liu, Y. Zhang, J. Zhou, Y. Yu, and R. Jia, 2021: Spatiotemporal characteristics of urban dry/wet islands in China following rapid urbanization. *J. Hydrol.*, **601**, 126618, <https://doi.org/10.1016/j.jhydrol.2021.126618>.
- Meili, N., A. Paschalis, G. Manoli, and S. Fatichi, 2022: Diurnal and seasonal patterns of global urban dry islands. *Environ. Res. Lett.*, **17**, 054044, <https://doi.org/10.1088/1748-9326/ac68f8>.
- NOAA (National Oceanic and Atmospheric Administration), 2023: Integrated Surface Database (ISD). Accessed 8 March 2023, [http://www.wpc.ncep.noaa.gov/html/heatindex\\_equation.shtml](http://www.wpc.ncep.noaa.gov/html/heatindex_equation.shtml).
- O’Gorman, P. A., and J. G. Dwyer, 2018: Using Machine Learning to Parameterize Moist Convection: Potential for Modeling of Climate, Climate Change, and Extreme Events. *J. Adv. Model. Earth Syst.*, **10**, 2548–2563, <https://doi.org/10.1029/2018MS001351>.

- Reichstein, M., G. Camps-Valls, B. Stevens, M. Jung, J. Denzler, N. Carvalhais, and Prabhat, 2019: Deep learning and process understanding for data-driven Earth system science. *Nature*, **566**, 195–204, <https://doi.org/10.1038/s41586-019-0912-1>.
- Schoen, C., 2005: A new empirical model of the temperature–humidity index. *J. Appl. Meteorol.*, **44**, 1413–1420, <https://doi.org/10.1175/JAM2285.1>.
- Si, M., Z. Li, F. Nerry, B. Tang, P. Leng, H. Wu, X. Zhang, and G. Shang, 2022: Spatiotemporal pattern and long-term trend of global surface urban heat islands characterized by dynamic urban-extent method and MODIS data. *ISPRS-J. Photogramm. Remote Sens.*, **183**, 321-335, <https://doi.org/10.1016/j.isprsjprs.2021.11.017>.
- Venter, Z. S., T. Chakraborty, and X. Lee, 2021: Crowdsourced air temperatures contrast satellite measures of the urban heat island and its mechanisms. *Sci. Adv.*, **7**, eabb9569, <https://www.science.org/doi/10.1126/sciadv.abb9569>.
- Verdin, A., C. Funk, P. Peterson, M. Landsfeld, C. Tuholske, and K. Grace, 2020: Development and validation of the CHIRTS-daily quasi-global high-resolution daily temperature data set. *Sci. Data*, **7**, 1–14, <https://doi.org/10.1038/s41597-020-00643-7>.
- Wan, Z., S. Hook, and G. Hulley, 2015: MYD11A1 MODIS/Aqua Land Surface Temperature/Emissivity Daily L3 Global 1 km SIN Grid V006. <https://doi.org/10.5067/MODIS/MYD11A1.006>.
- Weinberger, K. R., A. Zanobetti, J. Schwartz, and G. A. Wellenius, 2018: Effectiveness of National Weather Service heat alerts in preventing mortality in 20 US cities. *Environ. Int.*, **116**, 30–38, <https://doi.org/10.1016/j.envint.2018.03.028>.
- Yoo, C., J. Im, S. Park, and L. J. Quackenbush, 2018: Estimation of daily maximum and minimum air temperatures in urban landscapes using MODIS time series satellite data. *ISPRS-J. Photogramm. Remote Sens.*, **137**, 149–162, <https://doi.org/10.1016/j.isprsjprs.2018.01.018>.